Strain and damage build-up in irradiated crystals : Coupling X-ray diffraction with numerical simulations

Alexandre Boulle, A. Chartier, J.-P. Crocombette, T. Jourdan, S. Pellegrino, A. Debelle

Strain and damage build-up in irradiated crystals : Coupling X-ray diffraction with numerical simulations

A. Boulle[1], A. Chartier[2], J. -P. Crocombette[3], T. Jourdan[3], S. Pellegrino[4], A. Debelle[5]

[1]Institut de Recherche sur les Céramiques, CNRS UMR 7315, Limoges, France

[2]CEA, DEN, DPC, SCCME, Gif-Sur-Yvette, France.

[3]CEA, DEN, SRMP, Gif-sur-Yvette, France.

[4]CEA, DEN, SRMP, Laboratoire JANNUS, Gif-sur-Yvette, France.

[5]Centre de Sciences Nucléaires et de Sciences de la Matière, Université Paris-Sud, CNRS/IN2P3, UMR 8609, Université Paris-Saclay, Orsay, France.

Abstract

Radiation damage in materials is a space and time multi-scale process, ranging from the atomic scale up to the macroscopic scale, and from the femtosecond up to several years. The prediction of the long term evolution of materials subjected to radiative environments (in the nuclear or in the space industry, as well as in the field of microelectronics) therefore requires the combination of several simulation and experimental techniques able to cover the different space and time scales involved. X-ray diffraction (XRD) is highly sensitive to atomic displacements while probing macroscopic volumes of material. In this respect it is perfectly suited for the study of radiation damage. In this work it is shown how XRD can be quantitatively and qualitatively used in combination with numerical simulations, like molecular dynamics and rate-equation cluster dynamics, to analyze damage build-up in irradiated SiC and ZrC single crystals. Particular emphasis is laid on the methodological aspects of XRD data treatment in order to extract parameters such as damage-induced strain and disorder.

1. Introduction

The effects of irradiation in materials are inherently space and time multi-scale processes in the sense that the elementary events associated with energy transfer occur at the atomic scale and last from a few femtoseconds to a few picoseconds, whereas prolonged exposure to radiation might lead to macroscopic consequences such as amorphization, swelling, etc [1]. In the ballistic regime, the elementary event is the collision of an incident particle (ion, electron) with an atom of the target material which, if the transfer of kinetic is sufficient, might leave its initial site (hence, leaving a vacancy behind) and collide with one or several other atoms of the material and relocate in an interstitial position of the crystal. Most of the Frenkel pairs thereby created recombine by the end of

the collisional events, although some of these defects may survive and agglomerate as a result of the accumulation of such collision cascades. Complex microstructural phenomena involving defect clustering, defect coalescence and defect migration further lead to the macroscopic consequence above-mentioned [1]. The prediction of the long term evolution of materials subjected to harsh, radiative environments (*e.g.* in the nuclear or in the space industry, as well as in the field of microelectronics) therefore requires the combination, on the basis of physically relevant scenarios, of several simulation techniques able to cover the different space and time scales involved [2]. In this respect, being able to qualitatively and quantitatively confirm the computationally predicted damage buildup mechanisms using adapted experimental techniques is of utmost importance.

On this way, an obvious choice is transmission electron microscopy (TEM), mainly because of its atomic – scale imaging capabilities. In particular, the possibility the directly compare experimental images with defect structure models obtained by molecular dynamics (MD) or *ab-initio* calculations [3, 4] makes TEM an inevitable tool to characterize radiation – induced defects. The main drawback of TEM is that it is not straightforward to obtain statistically relevant measurements. It is therefore often used in combination with techniques able to probe macroscopic volumes of material, such as Rutherford backscattering spectroscopy in channeling mode (RBS/C) and X-ray diffraction (XRD).

RBS/C is a popular technique among the physics of irradiation community (mostly because RBS requires ion beams which are obviously found at ion irradiation facilities).This technique allows to retrieve depth – resolved damage profiles, where the damage level is quantified through the so-called randomly displaced atom (RDA) parameter. An important limitation of RBS/C is that it is not straightforward to establish a connection between the number of RDAs and actual structural defects (although a recent study aimed at lifting this limitation by modeling RBS/C spectra on the basis of more and more realistic atomic structures [5]).

XRD does not suffer from this limitation and it has been used for several decades to quantify strain and disorder in irradiated or implanted materials [6-14]. X-ray diffractometers are easily found in almost any laboratory and the different theories describing XRD in crystals with defects are well established since the 1970s. Despite this, there have been only a few attempts to combine XRD and numerical simulation for the study of radiation damage. For example, Cherkashin *et al.* [15] and Rieutord *et al.* [14] respectively used finite element modeling and *ab initio* calculations to interpret XRD – derived lattice strain. Nordlund *et al.* [16] and Olsen *et al.* [3] made use of diffuse X-ray scattering combined with MD to identify radiation – induced defects in Si and Ni, respectively.

In this work we review our recent effort to combine XRD and numerical simulation for the study of radiation damage in ion irradiated single crystals. Although part of the results presented here have already been published elsewhere [17-19], in the present work we emphasize on the methodological

aspects which were not detailed in our previous publications and, because of space limitations, are often overlooked in scientific publications although this information is usually crucial to reproduce results by other researchers. The theoretical background is briefly recalled in section 2; section 3 is devoted to a detailed description of the essential steps required for XRD data acquisition and simulation. Finally, section 4, through the examples of irradiated SiC and ZrC, details how XRD can be used in combination with MD and rate – equation cluster dynamics (RECD) to determine the damage build-up mechanisms.

2. Theoretical background

The scattering from large perfect crystals is best described by the dynamical theory of diffraction [20]. In the case of distorted crystals, the dynamical theory is much more difficult to implement. Nonetheless, in the case of a slowly varying strain distribution, the Takagi – Taupin equations [21, 22] allow to compute the scattered intensity, and a simple recursive algorithm [23] can be used when the strain variation is confined in one dimension. Another possible approach is to make use of the kinematical theory of diffraction which, as compared to the dynamical theory, neglects multiple scattering and is therefore valid for weakly diffracting, disordered or nanoscale materials.

In a disordered crystal, each atom, with initial coordinate $\mathbf{r}$, is displaced by some vector $\mathbf{u}(\mathbf{r})$. The amplitude scattered by the crystal is obtained by adding the amplitudes scattered by individual atoms (*via* the atomic scattering factor, *f*) taking into account the phase shift induced by the difference in beam path between the waves scattered by different atoms [24]:

$$E(\mathbf{Q}) = \sum_{j=1}^{N} f_j(\mathbf{Q}) \exp\left\{\mathbf{Q}\left[\mathbf{r_j} + \mathbf{u}(\mathbf{r_j})\right]\right\} \tag{1}$$

where $\mathbf{Q}$ is the scattering vector and $Q = 4\pi \sin(\theta) / \lambda$, θ being half the scattering angle and λ the x-ray wavelength.

It is convenient to separate the displacement vector into a random component, $\delta\mathbf{u}(\mathbf{r})$ and a non random component:

$$\mathbf{u}(\mathbf{r}) = \nabla \mathbf{u}(\mathbf{r}) \cdot \mathbf{r} + \delta \mathbf{u}(\mathbf{r}) \tag{2}$$

where $\nabla\mathbf{u}(\mathbf{r})$ is the Jacobian of the displacement (or the displacement gradient tensor):

$$\nabla \mathbf{u} = \begin{pmatrix} \partial u_x/\partial x & \partial u_x/\partial y & \partial u_x/\partial z \\ \partial u_y/\partial x & \partial u_y/\partial y & \partial u_y/\partial z \\ \partial u_z/\partial x & \partial u_z/\partial y & \partial u_z/\partial z \end{pmatrix} \tag{3}$$

For brevity, in the following we should refer to this tensor as the strain tensor, although it is important to note that in contrast to the actual strain tensor, $\mathbf{e} = (\nabla\mathbf{u} + \nabla\mathbf{u}^T) / 2$, the displacement gradient tensor includes rigid rotations, *i.e.* the off-diagonal components contain both shear strain and rigid rotations.

In the case of irradiated materials, the displacement is in general a sole function of the coordinate

perpendicular to the surface, noted z, whereas in the in-plane directions (x, y) the displacement is statistically homogeneous, so that the scattered radiation is actually an average over the atomic displacement probability distribution function. The quantity measured in an actual XRD experiment is the intensity

$$\langle E E^{*}\rangle = \langle E\rangle\langle E^{*}\rangle + \left\langle \left(E-\langle E\rangle\right)\left(E^{*}-\langle E^{*}\rangle\right)\right\rangle \tag{4}$$

where the fist term on the right hand side of the equation is the coherently diffracted intensity, I_{coh}, and the second term corresponds to the diffuse scattering intensity, I_{dif}, which are respectively written:

$$I_{coh}(\mathbf{Q}) = \left|\sum_j f_j(Q)\left\langle \exp\left[i\,\mathbf{Q}\,\delta\mathbf{u}(z_j)\right]\right\rangle \exp\left\{i\left[\mathbf{Q}\nabla\mathbf{u}(z_j)\right]\cdot\mathbf{r_j}\right\}\exp\left(i\,\mathbf{Q}\cdot\mathbf{r_j}\right)\right|^2 \tag{5}$$

$$I_{dif}(\mathbf{Q}) = \sum_j\sum_k f_j(Q) f_k^{*}(Q)\times\left\{\left\langle \exp\left[i\,\mathbf{Q}\left[\delta\mathbf{u}(z_j)-\delta\mathbf{u}(z_k)\right]\right]\right\rangle - \left\langle \exp\left[i\,\mathbf{Q}\,\delta\mathbf{u}(z_j)\right]\right\rangle\left\langle \exp\left[i\,\mathbf{Q}\,\delta\mathbf{u}(z_k)\right]\right\rangle\right\} \times\exp\left\{i\left[\mathbf{Q}\nabla\mathbf{u}(z)\right]\cdot\left(\mathbf{r_j}-\mathbf{r_k}\right)\right\}\exp\left[i\,\mathbf{Q}\cdot\left(\mathbf{r_j}-\mathbf{r_k}\right)\right] \tag{6}$$

In equation (5), the exponential in angular brackets is the Debye-Waller (DW) factor and yields a lowering of the diffracted intensity [24]. The second exponential, containing the displacement gradient, yields a shift of the XRD peak. Equation (5) shows that the analysis of the diffracted intensity distribution allows to determine (i) the depth-resolved strain profile, $\nabla\mathbf{u}(z)$, and (ii) the depth-resolved damage profile quantified by the DW factor. The DW factor lies in the [0,1] range, where 1 corresponds to a perfect crystal, and 0 corresponds to a fully damaged crystal. It should be noted that the DW factor is a function of **Q** and it is, therefore, not an absolute measure of lattice disorder. Instead, it provides a convenient quantitative comparison of lattice damage in different samples, provided that the same lattice planes are probed in the XRD experiment. This will be further discussed in the next sections. The analysis of diffuse scattering, equation (6), provides information regarding the nature and the density of the defects [6-8]. Equation 6 is here given for completeness but it will not be discussed any further in the present article.

3. Methodology

3.1 Data acquisition

As the strain and damage profiles are retrieved by the simulation of XRD data (see section 3.2), the reliability of the result is tightly linked to the quality of the data. Below, we recall important aspects connected to data collection.

Choice of the diffractometer.

The key feature that allows to retrieve the actual strain/damage profiles from the diffracted intensity is the existence of interference fringes which must, hence, be clearly resolved in the experimental

data. In the case of *low strain levels and large irradiation depth* (μm scale), the interference fringes will be narrow and closely-spaced so that high-resolution is mandatory to resolve the interference features. A diffractometer with a parallel beam delivered by a 4-reflection monochromator and, optionally, a crystal analyzer is perfectly suited in such a case.

On the contrary, in the case of *high strain levels and low irradiation depth* (nm scale), the resolution conditions can be relaxed in order to enhance the beam intensity. Typically a 1- or a 2-reflection monochromator combined with a slit-based point detector or a position sensitive detector is well suited for such cases.

Intermediate cases will require individual testing. In any case, the resolution of the diffractometer should be measured by recording data from a pristine crystal (this quantity is required for the simulation).

Crystal alignment

The diffractometer should be equipped with an Eulerian cradle (or an equivalent combination of rotations) that allows to precisely align the sample in the three dimensions. In particular, since the width of the intrinsic rocking curves of perfect single crystals is in general of the order of a few thousandths of degrees wide, a misalignment of a few 0.001° is sufficient to produce large errors in the intensity of the Bragg peak from the unirradiated region of the crystal. On the contrary, the rocking-curve of the damaged area is in general much wider and is hence less sensitive to misalignment errors. Therefore, even a small misalignment of ~0.001° leads to an overestimation of the intensity scattered from the damaged region as compared to the Bragg peak, which may result in dramatic errors in the DW factor.

Scanning range

Finally, attention must be paid to the scanning range of the θ-2θ scans. The area around the Bragg peak should be scanned wide enough to include all the scattering from the damaged region, *i.e.* the recorded intensity should reach the background level on both sides of the Bragg peak (this information is also required for the simulation).

3.2 Data simulation

The strain and damage profiles can be retrieved by simulating the XRD data using the RaDMaX program [25]. The underlying theoretical principles and the program itself have been presented in details elsewhere [25,26] and will therefore not be recalled here. Instead, we provide a detailed step – by – step description of the program usage, with the aim of guiding users in the simulation process. As an example, we here make use of the case of an irradiated (cubic yttria-stabilized)

zirconium oxide crystal; the corresponding data can be found in the "Example" folder of the RaDMaX program, details regarding the sample were given in [26]. For each simulation step, the XRD curves are plotted in Fig. 1(a) along with the experimental data. The XRD data exhibit an intense peak on the high angle side corresponding to the diffraction from the unirradiated region of the crystal underneath the damaged region. An additional signal with neatly resolved interference fringes extends towards the low angle region indicating the existence of a dilatation gradient originating from the damaged region. Fig. 1(b,c) display the evolution of the strain and DW profiles for each step.

Step 1: adjusting the diffractometer and material parameters

After loading the data, the parameters of the diffractometer have to be adjusted to match the diffractometer characteristics:

- The wavelength, e.g. $\lambda = 1.5406$ Å
- The shape and width of the resolution fucntion of the diffractometer, which have been obtained by fitting the data from a virgin crystal with a bell – shaped function. Usual shapes such a Gaussian, a Lorentzian and a pseudo-Voigt function are available. This parameter may also serve to account for imperfect single crystals which might exhibit broad peaks. For instance, in the next section we address the case of ZrC which features unusually broad and asymmetric Bragg peaks. This has been accounted for using an asymmetric pseudo - Voigt function (split pseudo - Voigt). In the present example the function is a Gaussian and the width is 0.013°.
- The background level: it is obtained from the minimum intensity observed in the experimental data, provided that it has been scanned wide enough (see previous section). A value of 5×10^{-6} here gives a satisfactory result.

The material parameters have to be adjusted to match the crystal being analyzed:

- The nature of the crystal (ZrO_2)
- The Miller indices of the reflection (400).
- The symmetry and lattice parameters of the crystal (cubic, $a = 5.1456$ Å). The lattice parameter can be fine-tuned so that the peak position of the simulated curve exactly corresponds to the experimental data. This step is crucial since the Bragg peak of the unirradiated region of the crystal serves as a reference for the strain (position) and for the DW factor (intensity).

- step 2: adjusting the strain level

The default strain value (1 %), Fig. 1(b), is too high and the diffraction peak of the damaged region extends outwards the actual angular range. Reducing the value to 0.55 % allows the simulated peak to match the position of the experimental data, see curve (2). The position of the unirradiated region

is used as a reference, and the strain values are therefore given relatively to the lattice parameter of the virgin crystal. It should be noted that in the present case, both the strain and damage profiles are constrained to smoothly converge to the values of the virgin crystal (0% and 1, respectively).

- *step 3: adjusting the damage thickness*

Curve (2) in Figure 1(a) shows that the simulated curve exhibits too much fringes as compared to the experimental data. The fringe spacing is due to the beam path difference between waves scattered by regions of constant strain; hence, because of the reciprocal relation between real and reciprocal spaces, narrow spaced fringes indicate a large damage thickness. In the present case, the latter was decreased from 3500 Å to 2000 Å, see curve (3). It is in general recommended to have one or two additional fringes in the simulation, *i.e.* to slightly overestimate the damage thickness. This is necessary to ensure the convergence of the fitting procedure (the overestimation being compensated by the shape of the strain/damage profile).

- *step 4: adjusting the damage level*

The default value of the DW factor (1) yields an overestimation of the intensity of the damaged region. Reducing its value to 0.55, Fig. 1(c), allows to lower the intensity, see curve (4).

- *step 5: tuning the shape of the strain profile*

A closer examination of curve (4) shows that the width of the fringes located at the smallest 2θ values (hence corresponding to the largest strain) is significantly smaller than the experimental fringe. Considering the previous argument regarding the fringe spacing, this difference indicates that the region of maximum strain is too broad. Manually reducing the width of this region, Fig. 1(b), allows to get a very good starting point for the simulation, curve (5). It can be noted that this requires to also increase the DW factor. For this step it can be useful to consider complementary data (obtained by RBS/C or SRIM simulations) in order to adjust the shape of the strain profile. Such strain profiles can be directly imported in RaDMaX.

To compute the scattered intensity, the irradiated region is numerically divided into slices [26]. The number of slices should be chosen high enough in order not to degrade the shape of the computed curves and low enough in order not to prohibitively increase the computation time. In the present case, 80 slices provided good results, which (given the 200-nm damage thickness) corresponds to a depth resolution of 2.5 nm.

Finally, the shape of the strain/damage profiles is controlled with the number of basis (B-spline) functions that are used. This number should be high enough to render all the details of the actual strain/damage profiles, but not too high, otherwise, unphysical oscillations may appear during the

fitting procedure. In the present case, it was set to 8.

- *step 6: fitting*

Given that the guess strain/damage profiles obtained in the previous step are probably very close to the final solution, a simple least-square fitting allows to obtain this latter, see curve (6). The resulting strain and damage profiles are given as full lines in Fig 1 (b,c), respectively. It can be noted that the DW profile exhibits oscillations in the region of maximum damage. This is a general feature that reflects the uncertainty of the fitting induced by the unavoidable noise in the data. In general, such oscillations are not observed in the strain profiles which are more dependent on the location and width of the fringes and less on the absolute intensities, contrary to the DW factor (equation 5).

Finally, in the case where no good guess strain/damage profiles can be obtained by manually tweaking the profiles, one can make use of the a generalized simulated annealing algorithm implemented in RaDMaX. This algorithm randomly explores the parameter space so as to look for the best possible solution. A direct drawback is that this results in much longer computing times, and finding the solution might require to launch the fitting procedure several times.

3.3 Comments on the shape of the strain profiles

Contrarily to what is sometimes stated in the literature, it is possible to retrieve the true shape and absolute position of the strain profiles. This is illustrated in Fig. 2.

Fig. 2(a) shows simulated curves with the same symmetrical strain depth-profile located at different depths below the surface. It can be observed that, whereas the envelope remains roughly unchanged, the fine structure of the fringes changes significantly. In particular, when increasing depth, a high frequency signal appears as a modulation of the envelope. This signal comes from the interference between the waves scattered by the (unstrained) substrate and the (unstrained) region present at the surface.

Similarly, Fig. 2(b) shows a same asymmetrical strain profile but with two different orientations. As above, when the low strain tail extends towards the surface, it gives rise to interferences with the waves scattered by the underlying pristine crystal, which in turn results in an additional high frequency signal.

In order to be able to retrieve such features, high quality experimental data is required (high signal - to - noise ratio, high resolution and well aligned samples) and the simulation has to be close to perfect in order to match the fine features of the data. Even in the case of a perfect fit, the validity of the results should be crossed-check with a complementary technique. In any case, a poor fit will yield unreliable strain/damage profiles.

4. Examples

4.1 Molecular dynamics and XRD: strain and damage in irradiated SiC

The radiation resistance of SiC has been investigated for decades because of the potential of this material in several applications in the nuclear industry and for high-power and high-temperature electronics. Here, we focus on our previous study of (001)-oriented 3C-SiC single crystals irradiated with 100 keV Fe^+ ions [17]. Because of the high strain levels observed in this materials along with small irradiated thickness, an intense incident X-ray beam was required, so that the XRD experiments were carried out using synchrotron radiation at the BM2 beamline of the European Synchrotron Radiation Facility (Grenoble, France).

The simulation of the 002 and 004 θ-2θ scans of 3C-SiC are shown in Fig 3(a,b), respectively. The resulting strain and DW profiles are given in Fig. 3(c,d). The simulations are close to perfect so that the strain and damage profiles can be confidently considered as reliable. This is further confirmed by the fact that the strain profiles resulting from the independent simulations of the 002 and 004 reflections almost perfectly superimpose. The damage region extends over 120 nm with a maximum damage located ~ 30 nm below the surface. With increasing fluence (expressed in displacements per atom, dpa) the level of strain increases, reaching values as high as 8.5 %, whereas the DW factor decreases, indicating an increase of the lattice disorder.

Results of the accumulation of 10 keV collision cascades in a box containing 40 000 atom [27] were analyzed. Additional simulations were conducted using Frenkel pair accumulations (FPA) in a simulation box with 14 000 atoms following the methodology introduced in [28]. Because of the limited size of the MD simulation cells (9×9×9 and 6×6×6 nm^3 for CC and FPA methods, respectively) imposed by the computing capabilities, it is not directly possible to compute strain and damage profiles. However, since the strain and DW profiles retrieved from the simulation of XRD data are spatially resolved with a resolution of 2.5 nm, it is possible to compute the average strain and DW in regions with sizes comparable with the MD simulation cells. We here consider the evolution in a 10 nm wide region around the depth of maximum damage (~ 30 nm).

In order to extract the strain and DW from the MD cells, the MD data has been used to generate "powder diffraction" data using the Debye scattering equation [24]:

$$I(Q)=\sum_n \sum_m f_m f_n \frac{\sin(Q r_{mn})}{Q r_{mn}} \tag{7}$$

where r_{mn} is the distance between all pairs of atoms. The calculation has been performed with the Debyer program (https://debyer.readthedocs.io/). The resulting calculations for selected fluences are given in Fig. 4. With increasing fluence, the diffraction peaks of SiC are shifted towards lower

values of the scattering vector, indicating the development of a tensile strain. Concomitantly, the intensity of the Bragg peaks is lowered, which indicates an increase of the lattice disorder which, in the case of SiC, corresponds to the amorphization of the material. Focusing on the 004 reflection, the corresponding strain and DW can respectively be obtained with:

$$e_{zz} = \frac{d - d_0}{d_0} \tag{8}$$

$$DW = \sqrt{\frac{I}{I_0}} \tag{9}$$

where the d is the lattice spacing, I is the integrated intensity (*i.e.* the area) of the diffraction peak and the subscript 0 denotes the unirradiated crystal. The square root in equation (9) originates from the fact that the DW factor is defined using the diffracted amplitude, whereas the quantity measured here is the intensity. The lattice spacing is related to the scattering vector via $Q = 2\pi / d$.

The evolution of the volume swelling (*i.e.* 3 times the linear strain corrected for the Poisson expansion induced by the unirradiated region [17]) and of the DW with fluence using XRD data and MD data are displayed in Fig. 5. For both parameters, a remarkably good agreement is obtained between XRD and MD, especially taking into account the fact that no fitting parameter is used here. This good agreement provides a direct experimental validation of the amorphization scenario predicted by MD simulations. More specifically, the analysis of the data using a direct-impact / defect-stimulated model [17] reveals that the formation of amorphous cluster is dominant starting from 0.1 dpa, which corresponds to the saturation of elastic energy of the system; in other words, the relaxation of the elastic energy associated with distorted clusters is the driving force for amorphization. Above 0.15 dpa the agreement between MD-derived and XRD-derived strain is much less satisfactory; this is most likely due to a known limitation of the interatomic potential that, as the atomic distances deviate significantly from the perfect crystal, underpredicts the experimentally measured swelling of the amorphous [29]. This is further discussed in [17].

Let us now focus on the DW factor. According to equation (6), for a 00*l* reflection the DW factor is defined as follows:

$$\mathrm{DW} = \left\langle \exp\left[i Q_z \delta u_z \right] \right\rangle = \int d\,\delta u_z \cdot p(\delta u_z) \exp\left(i Q_z \delta u_z \right) \tag{10}$$

where the averaging is performed over the probability distribution function (pdf) of the random displacements, $p(\delta u_z)$. As already mentioned in section 2, the DW factor is a function of the vector Q, so that investigating different *hkl* reflections result in different values of DW. This is indeed observed in Fig. 3(d) where the DW factor of the 004 reflection is systematically lower than the value derived from the 002 reflection. Acording to equation (10) this dependence can be used to derive the function $p(\delta u_z)$ and further determine a damage value that can be used as an absolute

metric of disorder using XRD data.

The random displacement distribution is often assumed to be Gaussian-shaped. In the case of *thermal* disorder, lattice dynamics in the isotropic harmonic regime predicts a Gaussian distribution [30] which gives rise to the well-known result DW = exp(- Q^2 <u^2> / 2). However, such a description is not suited to describe the disorder induced by collision cascades in irradiated materials. Indeed, the process of energy dissipation of low-velocity projectiles leads to atomic disorder that is due to both atoms close to equilibrium lattice sites and atoms significantly displaced from a regular site. This situation, where some displacements are statistically much larger than the "average" displacement, are known as Lévy flights [31]. Assuming that $p(\delta u_z)$ can indeed be described by a Lévy-stable distribution, the DW factor can be written [18]:

$$\mathrm{DW} = \exp\left(-\frac{1}{2}|Q|^{\gamma}\sigma_u^{\gamma}\right) \tag{11}$$

where $\gamma \in (0,2]$ is the tail index that determines the shape of the distribution: $\gamma = 2$ corresponds to the Gaussian distribution, and distributions with $\gamma < 2$ exhibit heavy tails (asymptotically behaving as $\sim 1/|u|^{1+\gamma}$), like for instance the Lorentzian distribution ($\gamma = 1$) [31]. σ_u is the characteristic width of the distribution [32], whose definition varies depending on the value of γ; for instance, it corresponds to the standard deviation for $\gamma = 2$, and to the full-width at half-maximum for $\gamma = 1$. These parameters can be derived from the experimentally derived values for the 002 and the 004 reflections:

$$\sigma_u = \left[2\frac{\ln(DW_{002}) - \ln(DW_{004})}{|Q_{004}|^{\gamma} - |Q_{002}|^{\gamma}}\right]^{1/\gamma} = \left[2\frac{\ln(DW_{002}) - \ln(DW_{004})}{|Q_{002}|^{\gamma}(2^{\gamma} - 1)}\right]^{1/\gamma} \tag{12}$$

$$\gamma = \frac{\ln\left[\ln(DW_{004})\right] - \ln\left[\ln(DW_{002})\right]}{\ln|Q_{004}| - \ln|Q_{002}|} = \frac{\ln\left[\ln(DW_{004})\right] - \ln\left[\ln(DW_{002})\right]}{\ln(2)} \tag{13}$$

Unfortunately there is no general closed-form formula of the Lévy-stable distribution, so that it has to be generated numerically using a pseudo – random number generator [33]. The result of Eqs. (12) and (13) is displayed in Fig. 6(a) for several fluences. It can be observed that for increasing fluence, not only the width of distribution increases (indicating the overall increase of disorder), but also the tail of the distribution increases (indicating that the probability of Lévy flights increases). From these distributions, an absolute measure of disorder can be derived, for instance by determining the fraction of atoms undergoing a displacement larger than a given threshold distance d_{th}:

$$f_D^{XRD} = \int_{d_{th}}^{\infty} d\,\delta u_z \cdot p(d\,\delta u_z) = 1 - \int_0^{dth} d\,\delta u_z \cdot p(d\,\delta u_z) \tag{14}$$

This equation corresponds to the complementary cumulative distribution function (1 – cdf) and is

plotted in Fig. 6(a). The damage fraction can be directly determined from the figure for any threshold value. The corresponding value for a threshold distance equal to the size of the unit-cell is given in Fig. 6(b). For the sake of comparison, the loss of long-range order determined by Gao & Weber [27] using the same data as that presented above (i.e. MD-CC calculations) is also displayed. A remarkable agreement between both evolutions is observed, which not only validates the relevance of the XRD-derived disorder parameter but also provides an experimental validation of the MD simulations.

4.2 Rate equation cluster dynamics and XRD: strain profiles in irradiated ZrC

In the case of SiC, because of the limitations imposed by the size of the MD cells, the discussion was limited to the evolution of strain and DW at a fixed depth. However, meaningful information can be further obtained from the analysis of the whole depth – profile. This is discussed in the present section in the case of irradiated ZrC crystals.

(001)-oriented ZrC crystals were irradiated with 1.2 MeV Au^+ ions as described in details elsewhere [34]. X-ray diffraction experiments were conducted on a high-resolution laboratory equipment operating with the $CuK\alpha_1$ radiation of copper (λ = 1.5406 Å) [34]. It is important to note that the quality of the crystal is not optimal (with several large crystals disoriented with respect to each other) which results in poorly resolved interference fringes in the experimental data, Fig. 7(a). For this reason, it was not possible to achieve perfect simulations; as a consequence, absolute values of strain and damage will not be discussed here. Instead, we shall focus on the relative evolution of the strain depth-profile with fluence. As mentioned in section 3, the Bragg peak of the pristine crystal (not shown here) exhibits an unusual asymmetric shape which is also visible in the irradiated crystals. Although the exact origin of this asymmetry is not established, it is likely connected with the poor crystal quality. More importantly, this asymmetry has been successfully modeled by convoluting the calculated curve with an asymmetric pseudo-Voigt function in the RaDMaX software.

The strain depth-profiles retrieved from the simulations are given in Fig. 7(b). At first glance, the resulting evolution of the profiles looks more complex than the evolution observed in SiC. Let us consider the evolution of the strain at a given depth, say 200 nm. The level of strain first increases between 0.085 and 0.14 dpa, and then drops to smaller values when increasing the fluence further. It can be noticed that this strain relaxation phenomenon is initiated at the damage-peak initial location and then propagates deeper below the surface,which results in a shift of this peak towards larger depths.

Interestingly, this phenomenon is observed for a variety of materials which do not amorphize under irradiation, like ZrO_2, UO_2 and MgO [19]. In the case of UO_2 for instance, this strain relaxation has

been ascribed to the transformation of dislocation loops into a tangled network of dislocation lines [35]. Indeed, whereas dislocation loops produce homogeneous strain (*i.e.* a uniform dilatation of the lattice), lines induce essentially heterogenous strain (*i.e.* localized and randomly distributed strain). In the XRD data this effect is clearly visible since peak shifted is replaced by peak broadening [36]. We recently conjectured that this mechanism could be extended to other non-amorphizable materials where strain relaxation is observed.

In order to confirm this hypothesis and to reproduce the depth-resolved strain relaxation observed in ZrC, we conducted rate-equation cluster dynamics simulations using the CRESCENDO code [37] to obtain quantitative depth profiles of the defect populations (which is not possible with MD techniques). This code computes the evolution of the population of vacancy and interstitial clusters through their creation by irradiation and growth or shrinkage by emission or capture of single defects. We used the 1D version of the code which considers homogeneous slices of the material parallel to the irradiated surface allowing exchange of mobile clusters between adjacent slices. The properties of point defects in ZrC, *i.e.* their formation and migration energies as well as their tendency to cluster were obtained from *ab initio* density functional theory calculations [34]. It should be noted that the complete reproduction of the microstructure evolution of irradiated materials is a tremendous task because of the complexity and imbrication of the various phenomena taking place as well as the number of microstructural features one would have to consider. Thus, in order to apply the RECD framework to ZrC we made some simplifying assumptions which are discussed in details elsewhere [19,34]. The resulting depth resolved interstitial cluster concentration (at an ion fluence of 2×10^{15} ions/cm^2) is given in Fig. 8(a), for selected cluster sizes. It can be observed that the larger defect clusters are located close to the surface, whereas small defects are more deeply buried below the surface.

In ZrC it has been shown that vacancies are immobile at room temperature, and they remain as monovacancies. On the contrary, interstitials are highly mobile and immediately tend to cluster to form dislocation loops [38]. The elastic strain can hence be computed from defect concentration profiles from:

$$e(z)=N_V(z)V_V^{rel}+\sum_L N_L(z)\Delta V_L \tag{15}$$

where $N_V(z)$ and $N_L(z)$ are the depth resolved concentrations of vacancies and loops respectively. V_V^{rel} is the relaxation volume of vacancies, which is -0.1 atomic volume (Ω) in ZrC [19]. ΔV_L is the swelling induced by a dislocation loop. It is a function of the burgers vector, the loop size, the loop orientation, etc. However, in the present case since we are not seeking to reproduce the exact value of strain, we only consider (100) loops, so that the swelling is simply equal to the atomic volume times the number of interstitials in the loop. In order to mimic the transformation of dislocation loops into lines, we introduced intrinsic dislocation lines in the simulation box and we forced the

loops to be integrated into the dislocation line network everytime the two species went in contact. The computed strain profiles are displayed in Fig. 8(b). One can note a discrepancy regarding the depth scale (which is most likely due to the fact that the defect source term is fixed from SRIM-computed dpa profiles and the fact that defect clusters were assumed to be immobile [19]). On the contrary, the calculated strain values are close to those determined by XRD and above all, the two-step process of the strain evolution is very well reproduced: the initial strain buildup is followed by a strain relaxation mechanism which is initiated at the strain peak, *i.e.* where the largest defects are formed. Those defects are more likely to react with pre-existing dislocations in the crystal to form dislocation lines, hence the observed drop in the strain level in this region. With increasing fluence, the size of defects deeper in the irradiated layer e progressively increases which increases their probability to also transform into dislocation lines, leading to a progressive strain relaxation at larger depths.

5. Conclusions

XRD is a powerful tool to characterize the defect structure in irradiated crystals. Although the most exhaustive information is obtained from the analysis of the completed scattered intensity (coherent and diffuse scattering), the analysis of the coherent scattering obtained from simple θ-2θ scans already provides a wealth of information, especially regarding strain and in disorder. Provided that high-quality data is recorded (high signal-to-noise ratio and sufficient resolution to resolve interference fringes), the absolute shape of depth – resolved strain and disorder profiles can be retrieved. Benefiting from the high spatial resolution (a few nm, depending on the simulation parameters), these strain and disorder profiles can be quantitatively compared with results obtained by atomic scale simulations, such as MD simulations, and hence confirm damage build-up scenarios. We have also shown that meso-scale simulations, like RECD for instance, allow to compute depth – resolved strain profiles that can be used in one – to – one comparison with experimental XRD results. In this latter example, a strain – relaxation mechanism involving the transformation of dislocation loops into dislocation lines has been evidenced.

References

[1] W. Wesh, E. Wendler, Ion Beam Modification of Materials, Springer Series in Surface Science 61 (2016) 3.

[2] K. Nordlund, F. Djurabekova, J. Comput. Eletron. 13 (2014) 122.

[3] R. J. Olsen, K. Jin, C. Lu, L. K. Béland, L. Wang, H. Bei, E. D. Specht, B. C. Larson, J. Nucl. Mater. 469 (2016) 153.

[4] C. Lu, K. Jin, L. K. Béland, F. Zhang, T. Yang, L. Qiao, Y. Zhang, H. Bei, H. M. Christen, R. E. Stoller, L.Wang, Sci. Rep. 6 (2016) 19994.

[5] S. Zhang, K. Nordlund, F. Djurabekova, Y. Zhang, G. Velisa, T. S. Wang, Phys. Rev. E 94 (2016) 043319.

[6] P. H. Dederichs, J. Phys. F 3 (1973) 471.

[7] B. C. Larson, W. Schmatz, Phys. Rev. B 10 (1974) 2307.

[8] B. C. Larson, W. Schmatz, Phys. Stat. Sol. (b) 99 (1980) 267.

[9] V. S. Speriosu, (1981). J. Appl. Phys. 52, 6094-6103.

[10] P. Zaumseil, U. Winter, F. Cembali, M. Servidori, Z. Sourek, Phys. Stat. Sol. (a) 100 (1987) 95.

[11] J. G. E. Klappe, P. F. Fewster, J. Appl. Cryst. 27 (1994) 103.

[12] S. Milita, M. Servidori, *J. Appl. Cryst.* **28** (1995) 666.

[13] A. Boulle, A. Debelle, *J. Appl. Cryst.* **43** (2010) 1046.

[14] F. Rieutord, F. Mazen, S. Reboh, J. D. Penot, L. Bilteanu, J. P. Crocombette, V. Vales, V. Holy, L. Capello, *J. Appl. Phys.* **113** (2013) 153511.

[15] N. Cherkashin, S. Reboh, A. Lubk, M. J. Hÿtch, A. Claverie, Appl. Phys. Expr. 6 (2013) 091301.

[16] K. Nordlund, U. Beck, T. H. Metzger, J. R. Patel, Appl. Phys. Lett. 76 (2000) 846.

[17] A. Debelle, A. Boulle, A. Chartier, F. Gao, W. J. Weber, Phys. Rev. B 90 (2014) 174112.

[18] A. Boulle, A. Debelle, Phys. Rev. Lett. 116 (2016) 24551.

[19] A. Debelle, J. -P. Crocombette, A. Boulle, A. Chartier, T. Jourdan, S. Pellegrino, D. Bachiller-Perea, D. Carpentier, J. Channagiri, T. -H. Nguyen, F. Garrido, L. Thomé, Phys. Rev. Mater. 2 (2018) 013604.

[20] A. Authier, Dynamical Theory of X-Ray Diffraction, Oxford Science Publications (2003)

[21] S. Takagi, *J. Phys. Soc. Jpn* **26** (1969) 1239.

[22] D. Taupin, *Bull. Soc. Franç. Minér. Crist.* **87** (1964) 469.

[23] W. J. Bartels, J. Hornstra., D. J. W. Lobeek, *Acta. Cryst. A* **42** (1986) 539.

[24] B. E. Warren, X-ray diffraction, Addison-Wesley 1(969).

[25] M. Souilah, A. Boulle, A. Debelle, J. Appl. Cryst. 49 (2016) 311.

[26] A. Boulle, A. Debelle, J. Appl. Cryst. 43 (2010) 1046.

[27] F. Gao, W. J. Weber, Phys. Rev. B 66 (2002) 024106.

[28] J.-P. Crocombette, A. Chartier, and W. J. Weber, Appl. Phys. Lett. 88 (2006) 051912.

[29] F. Gao, W. J. Weber, Phys. Rev. B 63 (2000) 054101.

[30] K. N. Trueblood, H. B. Bürgi, H. Burzlaff, J. D. Dunitz, C. M. Gramaccioli, H. H. Schulz, U. Shmueli, S. C. Abrahams, Acta. Cryst. A 52 (1996) 770.

[31] W. Feller, An Introduction to Probability Theory and its Applications, New York: Wiley (1970).

[32] A. Boulle, R. Guinebretière, A. Dauger, J. Phys. D: Appl. Phys. 38 (2005) 3907.

[33] J. M. Chambers, C. L. Mallows, B. W. Stuck, J. Am. Stat. Assoc. 7 (1976) 340.

[34] S. Pellegrino, J.-P. Crocombette, A. Debelle, Th. Jourdan, L. Thomé, Acta Mater. 102 (2016) 79.

[35] A. Chartier, C. Onofri, L. Van Brutzel, Ch. Sabathier, O. Dorosh, J. Jagielski, Appl. Phys. Lett. 109 (2016) 181902.

[36] A. Debelle, S. Moll, B. Décamps, A. Declémy, L. Thomé, G. Sattonnay, F. Garrido, I. Jozwik, J. Jagielski, Scripta Mater. 63, (2010) 665.

[37] T. Jourdan, G. Stoltz, F. Legoll, L. Monasse, Comp. Phys. Comm. 207 (2013) 170.

[38] L. Van Brutzel and J.-P. Crocombette, Nucl. Instrum. Methods Sect. B 255, 141 (2007).

Figure captions

Figure 1: (a) the different steps of the simulation of the 004 reflection of an irradiated ZrO_2 crystal (gray circles: experimental data; colored lines: simulation). The curves labeled (1) to (6) correspond to the different steps outlined in the text. The data are offset vertically for clarity. (b) and (c) respectively correspond to strain and DW profiles for each simulation step, using the same color coding as in (a). The final simulation results are shown as a solid line.

Figure 2: simulated XRD profiles of the 004 reflection of ZrO_2 corresponding to the strain profiles displayed in the inset. (a) The strain profiles only differ by the position of the maximum strain. The red, green and blue curves correspond to an increased depth below the surface. (b) The strain profiles have the same shape but a reverse asymmetry.

Figure 3: the 002 (a) and 004 (b) reflections of irradiated 3C-SiC (gray circles: experimental data; colored lines: simulation) for increasing fluence. The data are offset vertically for clarity. (c) and (d) respectively correspond to the retrieved strain and DW profiles using the same color coding as in (a) (black, blue, green, red for increasing fluence). Solid lines: simulation results of 002; dotted lines: simulation result of 004.

Figure 4: (a) XRD diagrams generated from the MD simulation cells using the Debye scattering equation (Equation 7) for several selected fluences. All peaks are labeled using the *hkl* indices of the 3C-SiC phase. (b) zoom on the 004 peak.

Figure 5: evolution of strain (a) and DW factor (b) obtained by XRD from a 10 nm – wide region (red squares), and by MD calculations using collision cascades (black circles) and Frenkel pair accumulation (white circles).

Figure 6: (a) evolution of the probability distribution function of atomic displacements pdf(u) (solid lines, left axis) computed using the values of σ_u and γ given by equation 12 and 13; evolution of the corresponding complementary cumulative distribution function 1 - cdf(u) (dotted lines, right axis). The same color coding as in figure 3 is used. (b) evolution of the XRD - derived damage fraction, f_D, obtained from equation (14) for a threshold distance equal to one unit cell (grey data). The loss of long-range order obtained by MD simulations is shown as the black line.

Figure 7: (a) the 004 reflection of irradiated ZrC as a function of ion fluence (gray circles: experimental data; colored lines: simulation). The data are offset vertically for clarity. (b) retrieved

strain profiles using the same color coding as in (a) (black, blue, green, red for increasing fluence).

Figure 8: (a) depth distribution of the concentration of clusters, $N_L(z)$, of selected sizes as calculated by RECD at a given fluence. (b) evolution with increasing fluence of the RECD-derived strain depth - profiles using equation 15. The same color coding as Fig. 7 is used.

Fig. 1

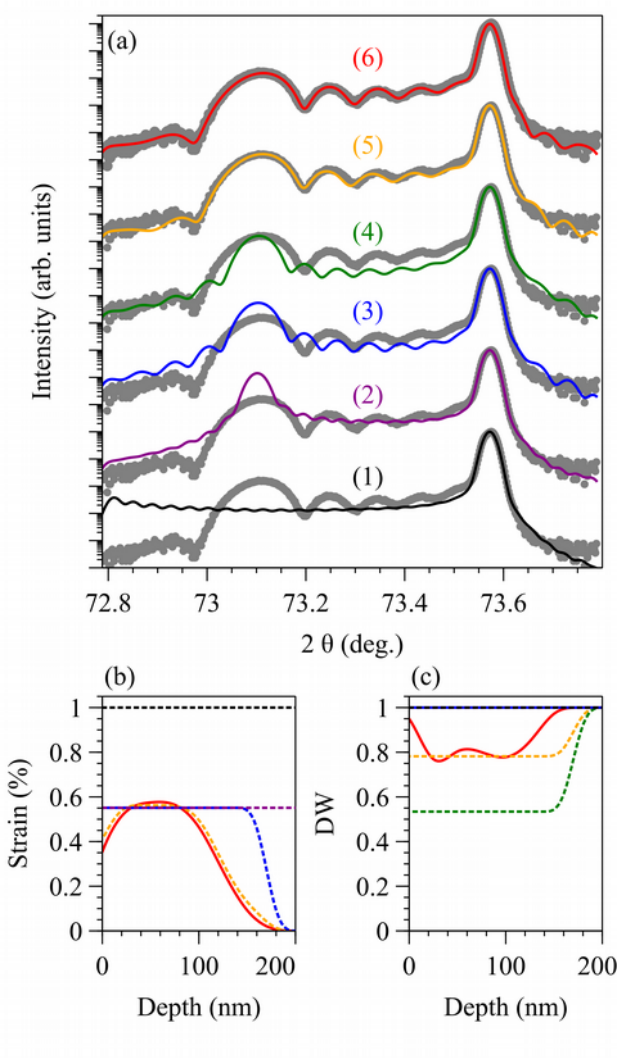
(a)
(6)
(5)
(4)
(3)
(2)
(1)
Intensity (arb. units)
72.8
73
73.2
73.4
73.6
2 θ (deg.)
(b)
Strain (%)
1
0.8
0.6
0.4
0.2
0
0
100
200
Depth (nm)
(c)
DW
1
0.8
0.6
0.4
0.2
0
0
100
200
Depth (nm)

Fig. 2

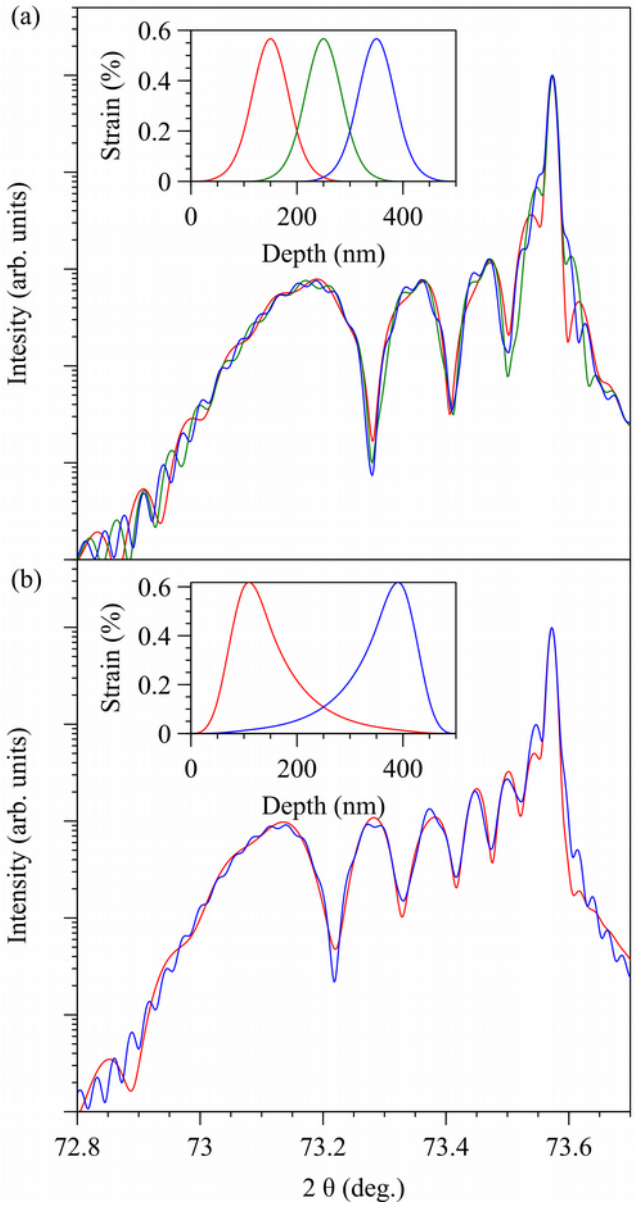
(a)
Strain (%)
0.6
0.4
0.2
0
0
200
400
Depth (nm)
Intesity (arb. units)
(b)
Strain (%)
0.6
0.4
0.2
0
0
200
400
Depth (nm)
Intensity (arb. units)
72.8
73
73.2
73.4
73.6
2 θ (deg.)

Fig. 3

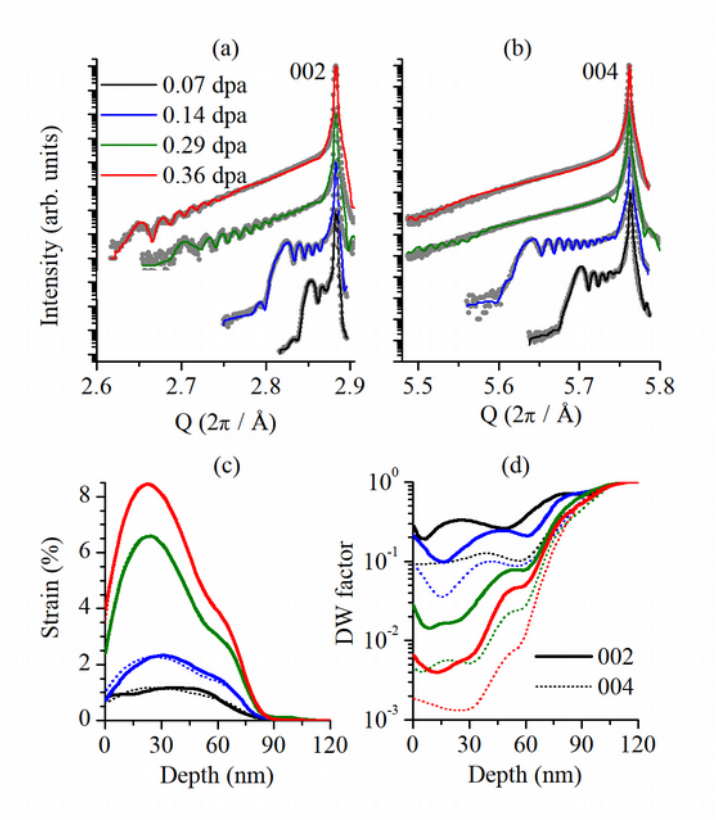
(a)
002
0.07 dpa
0.14 dpa
0.29 dpa
0.36 dpa
Intensity (arb. units)
2.6
2.7
2.8
2.9
Q (2π / Å)
(b)
004
5.5
5.6
5.7
5.8
Q (2π / Å)
(c)
Strain (%)
0
2
4
6
8
0
30
60
90
120
Depth (nm)
(d)
DW factor
10^0
10^{-1}
10^{-2}
10^{-3}
002
004
0
30
60
90
120
Depth (nm)

Fig. 4

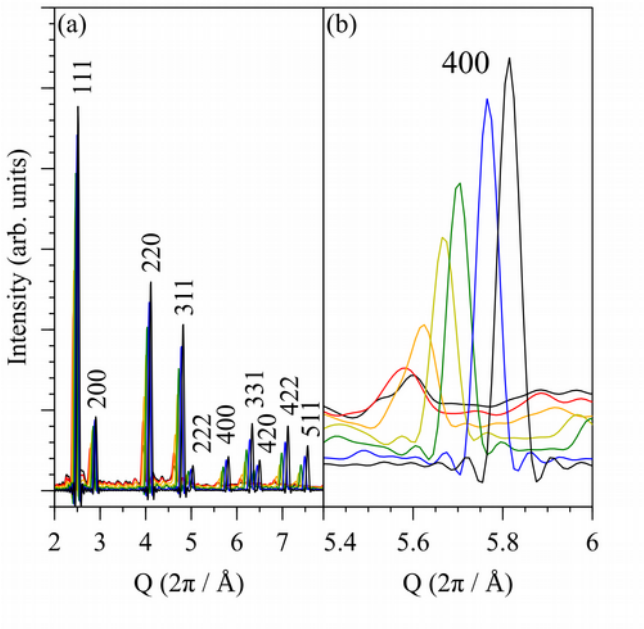
(a)
(b)
111
200
220
311
222
400
331
420
422
511
400
Intensity (arb. units)
2
3
4
5
6
7
5.4
5.6
5.8
6
Q (2π / Å)
Q (2π / Å)

Fig. 5

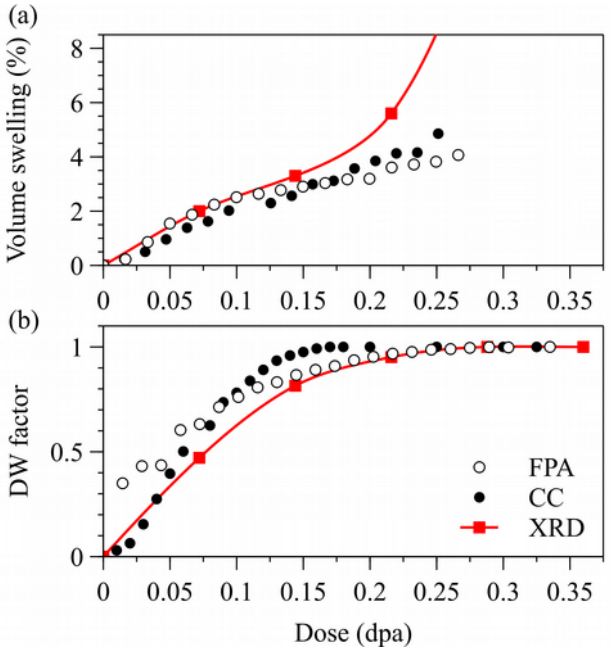
(a)
Volume swelling (%)
8
6
4
2
0
0
0.05
0.1
0.15
0.2
0.25
0.3
0.35
(b)
DW factor
1
0.5
0
FPA
CC
XRD
Dose (dpa)

Fig. 6

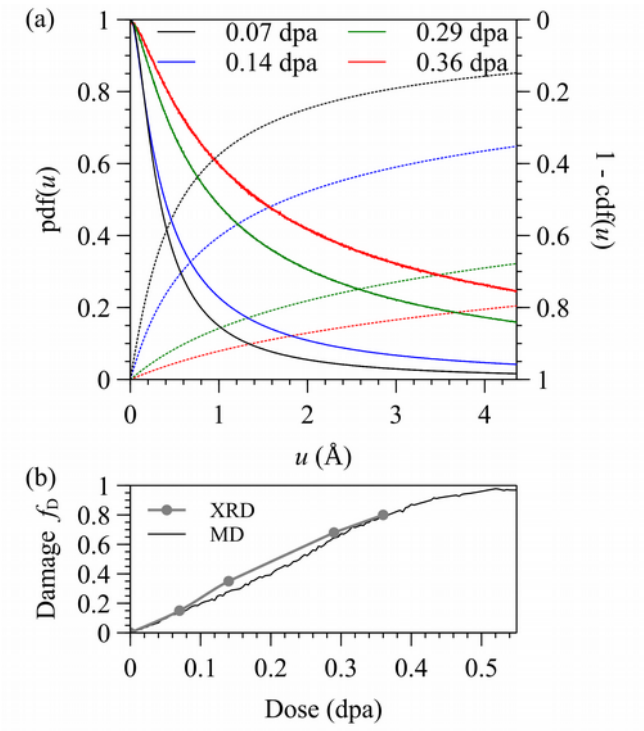
(a)
0.07 dpa
0.14 dpa
0.29 dpa
0.36 dpa
pdf(u)
1 - cdf(u)
u (Å)
(b)
XRD
MD
Damage f_D
Dose (dpa)

Fig. 7

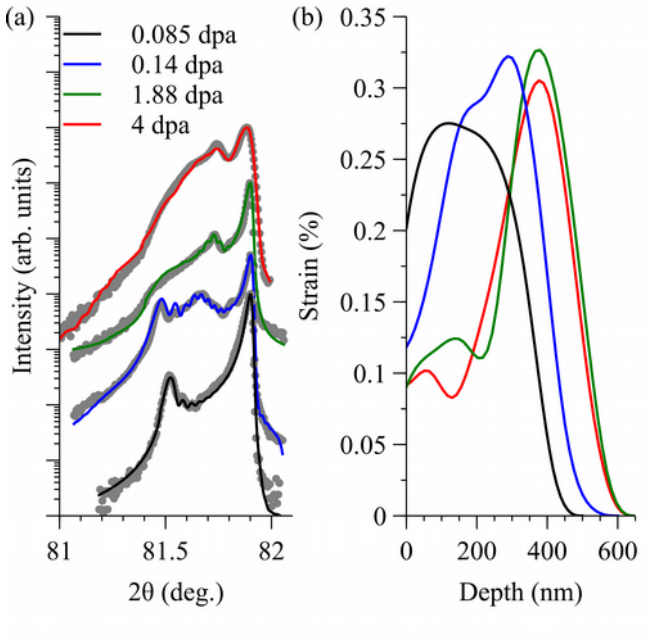
(a)
0.085 dpa
0.14 dpa
1.88 dpa
4 dpa
Intensity (arb. units)
81
81.5
82
2θ (deg.)
(b)
0.35
0.3
0.25
0.2
0.15
0.1
0.05
0
Strain (%)
0
200
400
600
Depth (nm)

Fig. 8

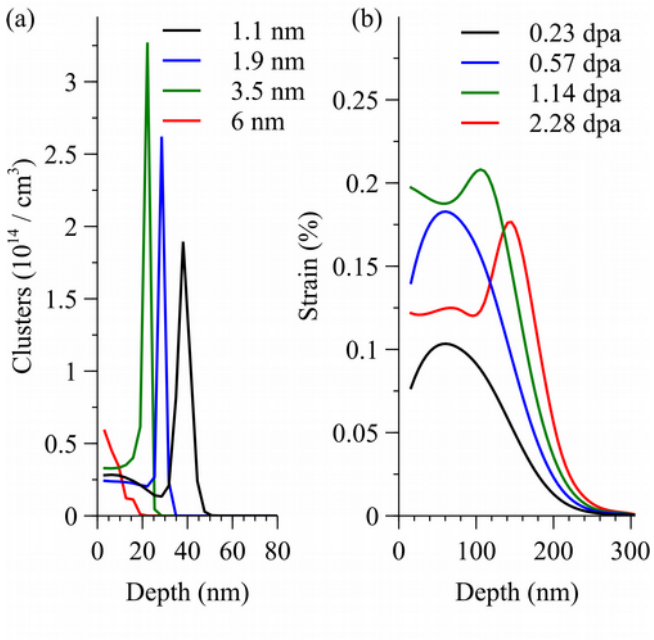
(a)
1.1 nm
1.9 nm
3.5 nm
6 nm
Clusters (10^{14} / cm^3)
Depth (nm)
(b)
0.23 dpa
0.57 dpa
1.14 dpa
2.28 dpa
Strain (%)
Depth (nm)